applied optics

Analysis and characterization of high-resolution and high-aspect-ratio imaging fiber bundles

Nojan Motamedi,* Salman Karbasi, Joseph E. Ford, and Vitaliy Lomakin

Department of Electrical and Computer Engineering, University of California San Diego, La Jolla, California 92093, USA
**Corresponding author: nomotame@ucsd.edu*

Received 22 July 2015; revised 3 October 2015; accepted 7 October 2015; posted 8 October 2015 (Doc. ID 246301); published 4 November 2015

High-contrast imaging fiber bundles (FBs) are characterized and modeled for wide-angle and high-resolution imaging applications. Scanning electron microscope images of FB cross sections are taken to measure physical parameters and verify the variations of irregular fibers due to the fabrication process. Modal analysis tools are developed that include irregularities in the fiber core shapes and provide results in agreement with experimental measurements. The modeling demonstrates that the irregular fibers significantly outperform a perfectly regular "ideal" array. Using this method, FBs are designed that can provide high contrast with core pitches of only a few wavelengths of the guided light. Structural modifications of the commercially available FB can reduce the core pitch by 60% for higher resolution image relay. © 2015 Optical Society of America

OCIS codes: (110.0110) Imaging systems; (110.2350) Fiber optics imaging.

http://dx.doi.org/10.1364/AO.54.009422

1. INTRODUCTION

Imagers with curved focal planes have been shown to be superior in terms of performance compared to the conventional planar focal plane imagers, due to the lower aberration and simpler design with fewer optical elements [1]. Realization of curved focal planes is, however, challenging due to the fabrication difficulties associated with nonplanar surfaces. Although different groups have successfully demonstrated curved focal planes [2–4], and stretchable electronics [5–7] have been known as a potential solution to the challenging problem of curved focal plane fabrication, they either have large radius of curvature or more importantly have low resolution. Little attention has been paid to the curved image sensors, and the characteristics of the curved focal planes are far from the flat image sensors. Alternatively, imaging fiber bundles (FBs) can be shaped into a curved focal plane using microgrinding. Imaging FBs have been used in numerous applications including illumination, tomography, and endoscopy [8–11]. Recently, high-resolution imaging FBs have been used for compact wide-angle and high-resolution imaging applications [12–14] where the curved image plane is mapped onto the flat sensor plane or a secondary flat image plane using the FBs. The motivation of using FBs is to make the conventional imagers more robust and compact by taking advantage of monocentric lenses with curved image planes. Figure 1(a) shows the fiber-coupled imager's cross section cut along the fiber length. The image captured by the monocentric lens is formed on the curved side of the FB. The image is then relayed to the image sensor through the straight FB. Modeling, characterization, and optimization of these straight FBs have gained interest for integrated imaging applications. Tapered and nonstraight imaging FBs have also been used in the fiber-coupled imagers to achieve better system integration [15]. The focus of this work is on straight FBs. Figure 1(b) shows the scanning electron microscope (SEM) image of the fiber-coupled imager's cross section showing the FB along with the image sensor.

Fiber-coupled imager resolution is limited by the FB pitch, as state-of-the-art image sensors are able to oversample and resolve individual fibers. Furthermore, in order to avoid the moiré pattern associated with fiber-coupled imagers [16], proper design of finer FBs is required. Finer pitches of FB may be fabricated by tapering them further. However, the performance of FBs in terms of transmitting an image with a low cross talk at a fixed wavelength would also diminish. Poor impulse response of the FB would result in image blur and decreases the image resolution in this type of imagers.

A set of straight FBs with different spatial resolutions (pitch) varying from 2.5 to 1.0 μm are characterized experimentally by placing them on a USAF resolution chart and evaluating the transmitted image using broadband illumination. Impulse response measurements are also taken by focusing a coherent 612 nm laser light onto the core of a 2.5 μm FB under various angles of incidence to evaluate the light confinement.

Modal analysis has been used to analyze the core-to-core coupling of imaging fibers [17,18] for a lower index contrast FB (Δn: 0.05). The effect of disorder was studied in [17] for FBs with 3.2 and 4.5 μm pitches using coupled mode theory and by considering only the fundamental mode of the fibers. In

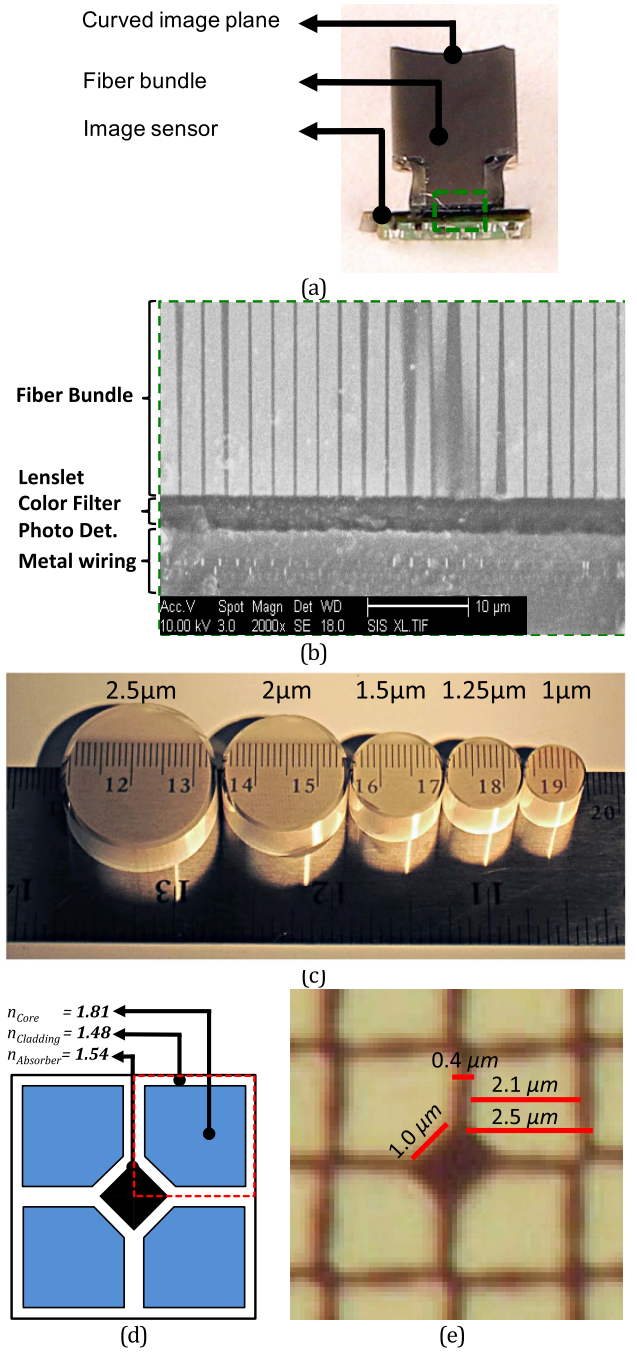

Fig. 1. (a) Fiber-coupled image sensor cut along the fibers; and (b) its SEM cross section. (c) Scaling of imaging FBs with different pitches. (d) Schematic of the five-sided FB cross section. (e) 76×-magnification optical microscope image of the FB.

this paper, entire guided modes of a 5 × 5 regular array of fibers are calculated numerically for a higher index contrast (Δn: 0.33) and finer pitches (1.5 μm) of FB. A Gaussian beam is propagated through the FB by calculating the overlap integral of the incident field and each guided mode. The effect of number of calculated modes and number of fibers in the simulation window is studied for more efficient modeling. An engineered irregularity is then introduced into the model to analyze its effect on the confinement of guided modes and impulse response of FB. Mode width diameter is calculated for each guided mode in both regular and irregular FBs to demonstrate higher confinement of irregular fibers. The modified model is then used to improve the performance of the FBs for higher spatial resolutions. An SEM cross-section image of the FB is introduced into the model to evaluate the performance of the actual FB for various pitches.

2. IMAGING FIBER BUNDLES

Various pitches of FBs may be fabricated by tapering and drawing them from an initially larger pitch. The fabrication process starts by drawing an individual fiber up to a certain width, cutting and stacking the individual drawn fibers, and redrawing them again. This process is repeated until desired length and pitch of the FB is reached. Schott's imaging FBs [19] are used throughout this paper for qualitative and quantitative analysis. Figure 1(c) shows the scaling of 10 mm long FBs with pitches from 2.5 to 1.0 μm. While the number of fibers does not change in each FB, its diameter decreases with the pitch. A schematic of FB cross section, as shown in Fig. 1(d), consists of a high index core, cladding, and extramural absorber material with real part refractive indices of 1.81, 1.48, and 1.54, respectively. The extramural absorber material is used for partial elimination of the background noise associated with radiation modes and cross talk between the fibers. Figure 1(e) is the optical microscope image of the 2.5 μm pitch FB. Extramural absorber material cannot be differentiated from cladding due to a lower refractive index contrast between the cladding and absorber.

Figures 2(a) and 2(b) show the SEM image of Schott's FB cross section with 2.5 μm pitch at 5000× and 15, 000 × magnification. An SEM image of a 1.0 μm pitch FB cross section was taken at 5000× and 12, 500 × for comparison. Scaling and physical structure of the 1.0 μm pitch FB with 2.5× higher magnification is similar to that of the 2.5 μm pitch FB.

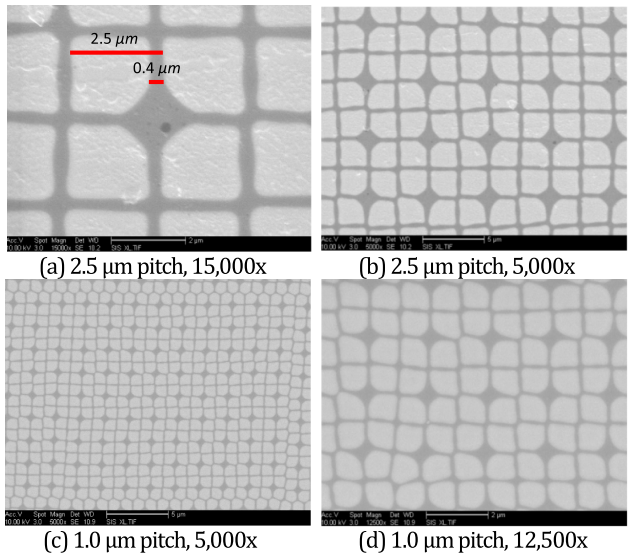

Fig. 2. (a), (b) SEM image of five-sided FB with a pitch of 2.5 μm at 15, 000 × and 5, 000 × magnifications; (c), (d) pitch of 1.0 μm at 5, 000 × and 12, 500 × magnifications.

SEM images of various pitches of FBs were converted to black-and-white images [Fig. 3(a)] for measurement and modeling purposes. The 2.5 and 1.0 μm pitch FBs of Fig. 1(c) were used for taking SEM data. The core area (white regions) percentage with respect to the total area of the FB's cross section was measured as a metric to ensure that the FB's structure is preserved for the 2.5 and 1.0 μm pitches. Three different SEM images were taken for each bundle pitch and the average core area was measured to be 69.3 and 69.1% for the 2.5 and 1.0 μm bundles, respectively. The measured core area percentages verify insignificant variation during the drawing process. The 69.1% and 69.3% core areas are close to the nominal core area of FB and are referred to as 70% core area in the rest of the paper.

In order to ensure that FB preserves its structure, that is, the core and cladding's shape, width, and scaling, an SEM image of a particular irregular area was taken from both input and output facets of a 10 mm long FB. Core boundary locations of the FB were extracted from the black-and-white image of the FB cross section at both facets. Otsu's thresholding method [20] was used to extract the black-and-white (binary) image from the gray-scale SEM image. The boundaries of black-and-white regions were registered as core boundaries. The core boundaries of both facets were then superimposed for comparison. Because the image of the output facet is a mirrored image of the same area on the input facet of the FB, one of the SEM images also has to be flipped in order to be directly comparable. Figure 3(b) shows the superimposed images of the FB's core boundaries. The flipped image of the core boundaries from the output facet (red lines) coincides well with the core boundaries from the input facet (white lines) after 10 mm of FB drawing with negligible variation in the size, shape, and location of individual fibers. This also validates the assumption of straight FB for modeling purposes.

3. CHARACTERIZATION OF FBS

Three types of measurements are taken for qualitative and quantitative characterization of FBs. Different pitches of FBs are placed on top of a resolution chart with bottom wide-angle white light illumination. The cross talk of transmitted images is compared. Then a 612 nm He–Ne laser is focused on the center of a 2.5 μm FB and the output intensity profile is recorded for different angles of incidence. Finally, a collimated white light source is used to assess the cross-talk width in various pitches of FBs and for different angles of incidence.

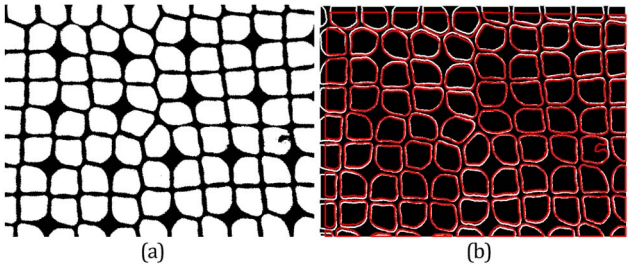

Fig. 3. (a) Conversion of SEM image to black (cladding and absorber regions) and white (core region). (b) Core boundaries obtained from the SEM image of five-sided FB with a pitch of 2.5 μm (white boundaries from side 1 and red boundaries from side 2 after 10 mm fiber drawing).

A. Qualitative Characterization

FBs with various pitches were placed on top of a USAF resolution chart as shown in Fig. 4. An index matching oil with refractive index of 1.6 was used between the FB and resolution chart to minimize scattering of light and the gap between the resolution chart and FBs. Figure 4(a) shows different pitches of the FBs ranging from 1.0 to 2.5 μm. As described in the previous section, finer pitches are fabricated by drawing the same array of fibers, and they all have the same 10 mm length. Figure 4(b) shows the 20× magnification image from the finest set of bars on the resolution chart under the same lighting conditions. The numerical aperture (NA) of the capturing microscope (Keyence VHX-1000) for this experiment was 0.48 with working distance of 25 mm. The width of one line in the six elements of groups 6 and 7 on the resolution chart varies from 7.81 μm to 4.38 μm and 3.91 μm to 2.19 μm, respectively. A partially collimated white light was used for all pitches. The individual fibers may be seen in the 2.5 μm, 2.0 μm, and even the 1.5 μm pitch FBs. Finer pitches of FBs are ideal for imaging applications if each individual fiber maintains the spatial properties of the image with minimized cross talk between adjacent fibers. However, scaling down the bundle pitch would lead to thinner cladding width at a fixed wavelength. Since the field decays exponentially outside the core region, a thinner cladding at a fixed wavelength would lead to a stronger field at the core–cladding interface of the adjacent fibers, thus increasing the cross talk between individual fibers. This explains why the 1.25 and 1.0 μm fibers do not maintain the same image quality as larger fiber pitches. Similar results were observed with higher NA objective (NA 0.9), and the lower confinement of FBs at finer pitches will be confirmed in our quantitative experiment in Section 3.C. Figure 4(c) shows the saturated image in the same region as in Fig. 4(b), where the exposure time was increased so that the aforementioned cross talk is more visible.

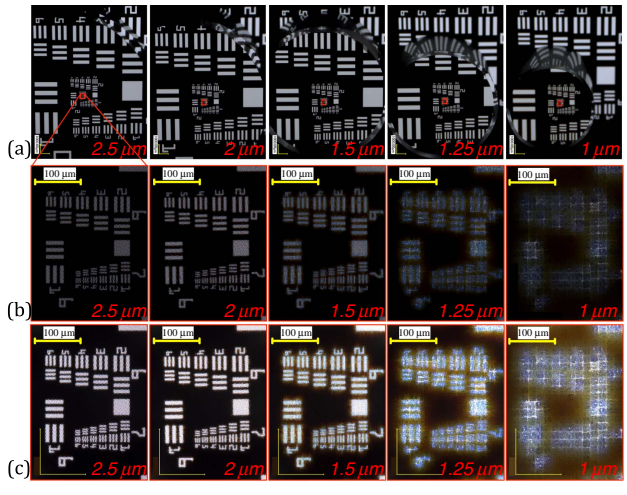

Fig. 4. Qualitative examination of scaling effect on the performance of FBs. (a) Different pitches of FBs on top of the resolution chart; (b) 20× magnification image passed through the 1 cm long FB; (c) the same image as in (b) but saturated to magnify the cross talk between the fiber cores.

B. Quantitative Characterization, Impulse Response

FBs are shift-variant optical elements and therefore the linear shift-invariant analysis cannot be applied. However, the optical impulse response measurements can give us an intuition about the performance of the FBs for image-transmitting applications. The transmission of a 2.5 μm pitch FB was measured by focusing a collimated He–Ne laser on the core of the FB using a microscope objective with NA of 0.42. The transmitted image was then captured using an optical microscope with NA of 0.48 on the other side of the FB. The He–Ne laser operated at a wavelength of 612 nm. The measured spot size (Airy disk diameter) of the launched beam was 2.1 μm, which is close to the theoretical diffraction-limited spot size of the microscope objective (1.8 μm). Figure 5(b) shows the saturated image of the focused laser light on the center of a fiber core with a white-light background to show the FB grid. The intensity profile of the beam in the back end of the FB in Fig. 5(c) shows no cross talk to the adjacent cores. The FB was then tilted for illumination at larger angles of incidence.

Figure 6 shows the FB's transmitted image for different angles of incidence. The exposure time was increased from 0.1to 0.5 ms for larger angles of incidence. Figure 6(b) is the corresponding X and Y plot of intensity for each angle of incidence with the center being the peak intensity. All figures are normalized by considering the exposure times and peak-intensity values. As the angle of incidence increases the transmitted intensity and power decreases due to low input and output coupling of light from the FB. Limited NA of the capturing objective would decrease the accuracy of calculations at larger angles of incidence. Because of the diffraction limit (1.8 μm) of the focusing objective, finer pitches of FBs cannot be characterized using this measurement technique. Moreover, FBs are highly shift-variant optical elements, such that the measurement setup is highly sensitive to vibrations and the results could not be regenerated reliably. Although this type of measurement demonstrates the confinement of 2.5 μm pitch FB, an alternative measurement technique is required to characterize the cross talk of FBs at finer pitches.

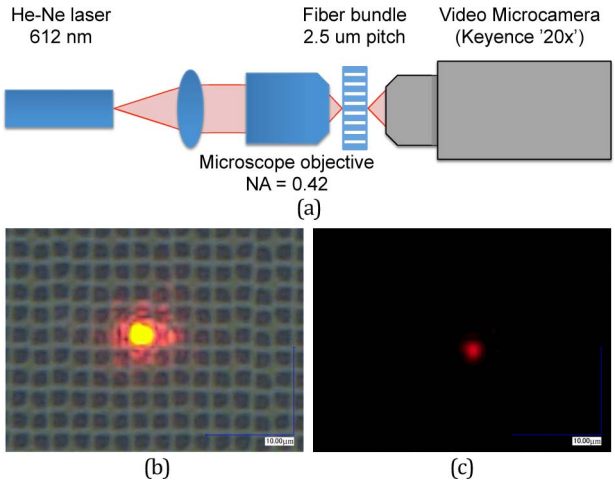

Fig. 5. (a) Schematic of impulse response measurement; (b) saturated focused laser light with white light background to illuminate the fiber grid; and (c) focused laser light on the center of the fiber core.

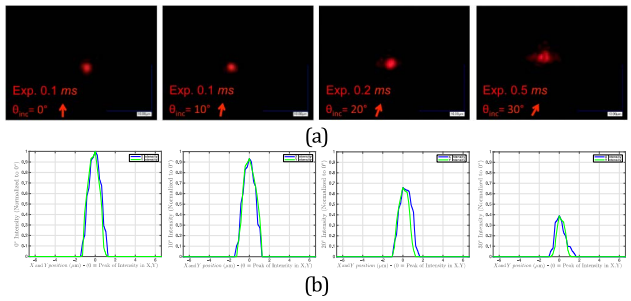

Fig. 6. Impulse response measurement at different angles of incidence. (a) 2D output intensity profile; and (b) normalized X (blue) and Y (green) intensity cross section centered at peak.

C. Quantitative Characterization, Slant-Edge Measurement

For more quantitative characterization of cross talk in the FBs an alternative measurement technique was used. The schematic of the measurement setup is shown in Fig. 7(a), where a bright white LED light source was placed against a 500 μm pinhole. An achromat lens was then placed at the distance equivalent to the lens focal length to create a collimated white light. The white LED light source was used in order to measure the average cross-talk value for all visible wavelengths as opposed to single wavelength characterization. FBs were placed on top of a USAF resolution chart and were illuminated by the collimated white light at three angles of incidence: 0°, 22.5°, and 45°. A high NA objective with NA of 0.9 was used to capture the transmitted image off the output surface of the FBs. Figure 7(b) shows the transmitted image of an edge through a 10 mm long FB with a pitch of 2.5 μm at normal incidence. In

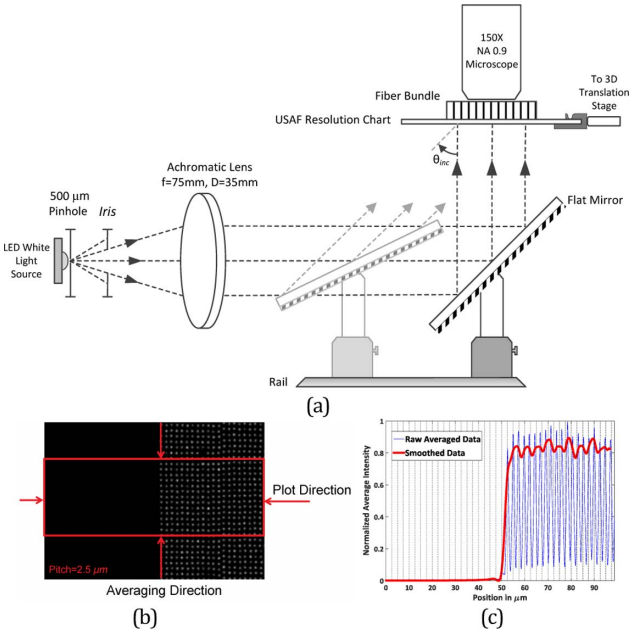

Fig. 7. (a) Schematics of the measurement setup: collimated white light incident on the FB on top of USAF resolution chart; (b) transmitted image of the edge through the FB at normal incidence; and (c) averaged intensity plot in the direction normal to the edge.

order to be able to measure the cross talk between individual fibers, the transmitted light was examined near the edge. Cross talk was quantified by first averaging the intensity of the transmitted image in the direction parallel to the edge over 500 pixels in the image, which is equivalent to physical length of 33 μm. This would compensate for the FB's defects and random variations in size and location as well as the intensity variations of the collimated light source. The averaged intensity was then plotted in the direction normal to the edge [Fig. 7(c)]. What appears in the background of the raw averaged data in the blue curve is in fact the effect of misalignment of fibers in each column (parallel to the edge) and the intensity fluctuation within each fiber. A smoothing spline curve fitting [21] was applied to the averaged data to get a smoother transition from the bright to dark region (red curve), as well as eliminating the intensity fluctuations between FBs due to their shift-variant property. The smoothing parameter was chosen such that the transition is smooth for calculating the intensity transition width from 80 to 10% of the peak. The same smoothing parameter (10^{-4}) was chosen to smoothen all measured data consistently. The cross-talk width varies depending on the value of the smoothing parameter, but the consistency of measurements is preserved for a constant value of smoothing parameter. This metric was used for measuring the cross talk between individual fibers at all pitches.

It is important to characterize the FBs for different angles of incidence in imaging applications, where a conventional lens is used to focus a cone of light on the image plane, which in this case is the FB's input facet. Figure 8(a) shows the transmitted image off a 10 mm long FB with 2.5 μm pitch at three different angles. All of the images were taken under the same lighting conditions, but the exposure time was increased from 3.2 to 16 s for higher angles of incidence. The intensity plots were normalized to the intensity of normal incidence image. At normal incidence, the overlap between the incident field and the lowest order modes of the individual fibers is high. As a result, the transmitted light through each FB appears as a combination of the first few lower-order modes. Since the lower-order modes of a multimode fiber are more confined, the transmitted light intensity is also higher at the center of the core and decays rapidly as it gets off the center. This would make the FB strongly shift variant at normal incidence. In the experimentally

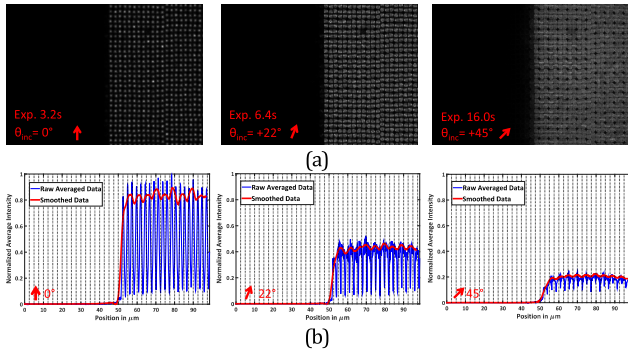

Fig. 8. (a) Transmitted image through 2.5 μm pitch FB at different angles of incidence; and (b) their average intensity plot in the direction normal to the edge.

demonstrated fiber-coupled imager [12], the transmitted image of the fiber will be sampled directly by an image sensor, which is shift variant itself. Therefore in the cases where the FB's pitch is comparable with the image sensor pitch a moiré pattern will be observed [16,22–24]. It has been shown that the moiré pattern can be reduced by proper image processing [16,22–24].

As the angle of incidence increases, higher-order modes of the fibers are excited as well as the lower-order modes. Since higher-order modes are less confined the transmitted light through the FB would be less shift variant. The transmitted intensity and power decreases by increasing the angle of incidence due to lower coupling into and from the FB. The absorber material also reduces the transmitted power due to a stronger field in the absorber at higher angles of incidence. These measurements are in agreement with the impulse response measurement. However, the slant edge measurement can be repeated reliably and for all pitches, and therefore it is a more suitable experiment for FB characterization. Figure 8(b) shows the intensity plot of the transmitted image of the edge through the FB in the direction normal to the edge for three different angles of incidence.

Table 1 shows the cross-talk width of different pitches of FBs for different angles of incidence. Due to shift-variant property of the FBs and smoothing curve fitting that was applied to the measured intensity, the measured cross-talk width is larger than the fiber pitch. The cross-talk width consistently increases for greater angles of incidence and finer pitches of FB. The positive and negative angles of incidence show the same degree of cross talk, but the cross-talk width is highly affected by the FB pitch. As the FB pitch decreases at the same wavelength, the decaying field in the cladding region gets stronger at the core–cladding interface of the adjacent fiber, leading to stronger cross talk between fibers after a certain threshold is reached. The measured cross talk is in agreement with the qualitative measurements presented in Section 3.A, where in both cases the finer pitches of the FBs show poor performance. In order to improve the performance of FBs at finer pitches one has to either increase the refractive index contrast between the core and cladding [25], which raises fabrication complications, or increase the cladding thickness to further suppress the field decay in the cladding region. The details of performance improvement of the FBs are discussed in the subsequent section.

4. MODELING OF IMAGING FIBER BUNDLES

The pitch of FBs varies from 1.0 μm to 2.5 μm (~2–5λ), while the length is on the order of millimeters (~$10^4\lambda$). Full-scale rigorous modeling of the FBs is, therefore, extremely hard due to the large aspect ratio and overall size. Although 2D modeling

Table 1. Cross Talk Width (μm) of Different Pitches of FBs for Various Incident Angles

Pitch/θ_{inc}	−45°	−22°	0°	22°	45°
1 μm	53.9	28.2	23.7	29.9	52.3
1.25 μm	29.2	21.2	21.8	20.7	33.9
1.5 μm	18.8	10.1	5.1	11.7	21.4
2 μm	16.4	4.7	2.5	6	13
2.5 μm	5.5	3.9	2.1	3.8	5.1

of FBs [26,27] (1D periodicity + propagation) provides an intuition of the scaling effect and cross talk, it may be inaccurate for quantitative 3D modeling of realistic FBs. Here we use an approach in which the modes of a finite size array of waveguides are calculated using the cross section of the actual FBs. This is achieved by introducing the SEM cross-section images of the FB into the model. The overlap integral between the incident beam and each of the guided modes is calculated to get the coupling coefficients. These coefficients are then used to calculate the transmitted beam at any length.

A. Formulation

The transmitted field at a desired propagation length inside the FB can be computed via modal superposition:

$$E_T(x,y,z) \approx \sum_m c_m E_m(x,y) e^{-jk_0 n_{\mathrm{eff},m} z}, \tag{1}$$

where $E_m(x,y)$ is the mth electric field mode profile of the FB, $n_{\mathrm{eff},m}$ is the mth mode effective index ($k_0 n_{\mathrm{eff},m}$ is the corresponding modal wavenumber), and c_m is the coupling coefficient to the mth mode. The modes are global in the sense that they include the coupling between all the (finite number of) fibers considered in the model. The summation in Eq. (1) is taken over the guided modes considering that for the long-range propagation studied here, the modal cross talk is dominated by the coupling between the guided modes, while all radiation/leaky modes are scattered out and are diminishing at the output plane.

The guided modes of the FB can be found numerically using a finite element method (FEM) or finite difference method. Here, the modes are found via FEM. The modal coefficients c_m are found by approximating the field at the incidence plane by the incident field, which assumes that the coupling of the incident beam into the FB is strong. This assumption is justified by the fact that we can often use a matching material. Additionally, a complete 2D (1D cross-section) analysis demonstrates that the propagation confinement results obtained with and without this assumption are similar. To this end, the incident field is expanded as [28]

$$E_{\mathrm{inc}} = \sum_m c_m E_m(x,y). \tag{2}$$

One can further multiply both sides of (2) by the complex conjugate of the nth magnetic field mode profile H_n^* and integrate the resulting power:

$$\iint (E_{\mathrm{inc}} \times H_n^*) \cdot e_z \mathrm{d}x\mathrm{d}y = \iint \left(\sum_m c_m E_m \times H_n^*\right).e_z \mathrm{d}x\mathrm{d}y, \tag{3}$$

where e_z is the unit vector in the propagation direction z. Using the mode orthogonality, the coefficients of the overlap integral can be written as

$$c_m = \frac{\iint (E_{\mathrm{inc}} \times H_m^*) \cdot e_z \mathrm{d}x\mathrm{d}y}{\int (E_m \times H_m^*) \cdot e_z \mathrm{d}x\mathrm{d}y}. \tag{4}$$

The integrals in Eq. (3) are calculated numerically based on the FEM solutions for the modes. With the coefficients in Eq. (3), the transmitted field is found via Eq. (1).

B. Analysis of Computation Parameters

Modal analysis of high-contrast FBs may be time consuming, and the computation time scales quadratically with the number of fibers. Therefore, proper choice of the number of calculated modes and the number of fibers kept in the computation domain is important. Depending on the illumination angular spectrum a lower number of modes may be used to calculate the propagated beam.

Root mean square error (RMSE) of normalized intensity of a 1.5 μm pitch FB after 0.5 mm propagation was calculated with different number of modes in a 5 × 5 array of fibers with 70% core area. RMSE was calculated from the following:

$$\mathrm{RMSE} = \sqrt{\iint (I_{\mathrm{exact}} - I_{\mathrm{apr.}})}, \tag{5}$$

where I_{exact} is the exact normalized output intensity calculated using all the guided modes and $I_{\mathrm{apr.}}$ is the normalized output intensity calculated using fewer number of guided modes approximation. The incident field is a Gaussian beam with a radius of 0.5 μm at a wavelength of 612 nm. The input Gaussian beam radius was chosen such that it mostly excites a single fiber at the input facet of the FB even for tilted inputs. The cross talk observed at the output is then strictly due to the coupling between fibers during propagation of light. For larger beam width, the coupling to the adjacent cores may occur because of the input coupling. Propagation length of 0.5 mm is long enough for observing the cross talk in the 1.5 μm pitch fiber array. Figure 9(a) shows the RMSE versus the number of modes for various angles of incidence. Small variation in the RMSE for smaller angles of incidence indicates that a smaller number of modes may be calculated for these cases. As the angle of incidence increases a larger number of modes is required to achieve the same error. Figures 9(b) and 9(c) show the transmitted beam at a distance of 0.5 mm for a normally incident Gaussian beam calculated with all (678) guided modes and with only the lowest three guided modes; a good agreement is obtained between these cases. On the other hand, for the 30° of incidence case [Figs 9(d) and 9(e)], a good agreement is obtained only with a larger number (169) of modes. Therefore, a fewer number of modes may be calculated depending on the launching condition and parameters of the FB.

Furthermore, to verify the effects of the number of fibers on the results, a larger array of fibers was modeled using the same modeling method. The binary image of 70% core area FB (from SEM measurement) was numerically eroded to 50% core area using the methods described in [29,30]. Figures 10(a) and 10(b) show a 9 × 9 array of the 1.5 μm pitch FB at the propagation distance of 0.5 mm for 70% and 50% core areas. The 70% core area FB shows a significant cross talk, and the intensity distributions of arrays with a different number of fibers differ due to the large field spread and finite size of the computational domain. On the other hand, the intensity distribution of the well-confined 50% core area FB is identical to that of the 5 × 5 array. One should note that as far as imaging applications are concerned, a confined impulse response is the most important characteristic of an imaging FB. Once the impulse response is not confined within one fiber, the image detected by the image sensor is blurred and the intensity

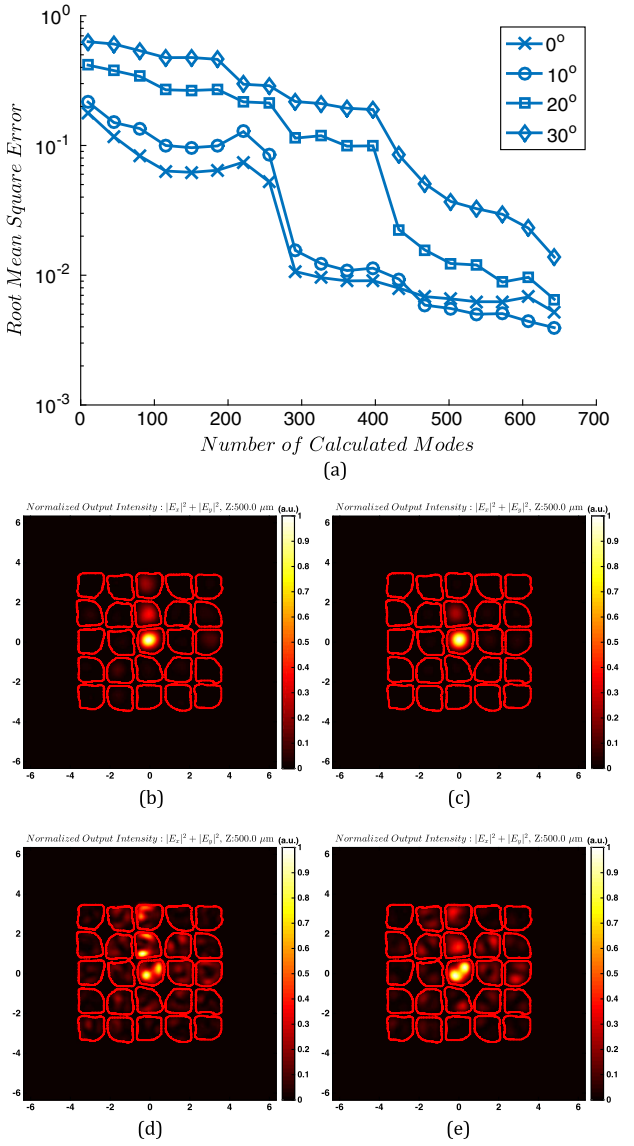

Fig. 9. RMSE for 5 × 5 array of fibers with 70% core area with 1.5 μm pitch, impact of number of calculated modes kept in calculations for different angles of incidence. (a) RMSE versus the number of modes; (b) the transmitted field for normal incidence with all of the 678 modes; and (c) with only 3 modes; (d) the transmitted field for 30° incidence with all the modes; and (e) with 169 modes.

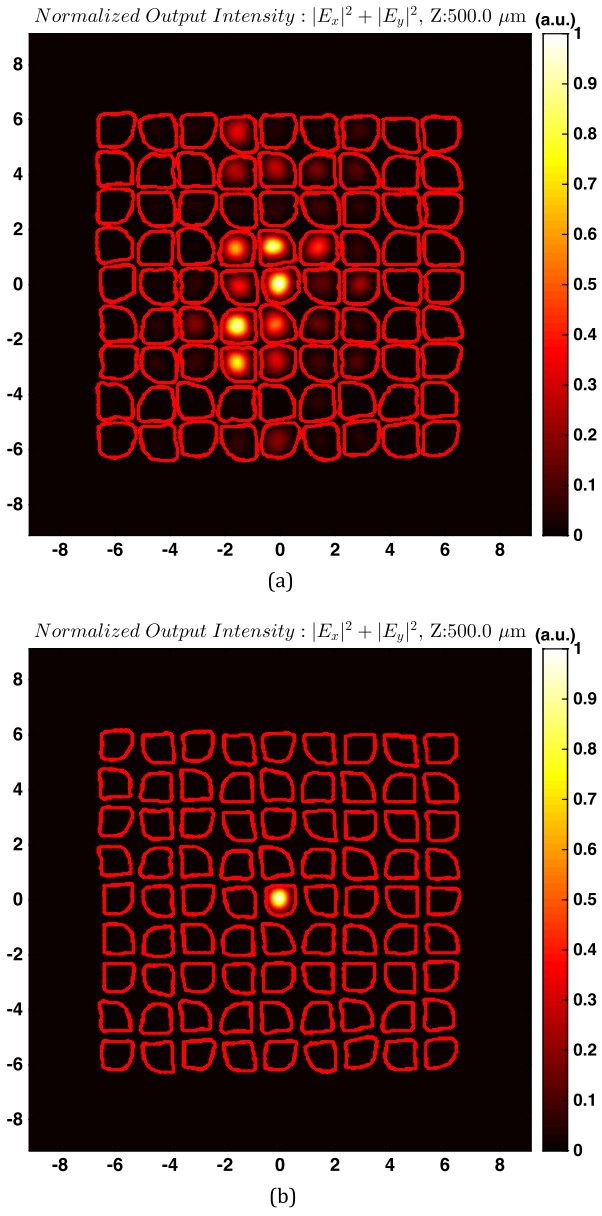

Fig. 10. Impulse response of a 9 × 9 array of fibers with 1.5 μm pitch for (a) 70% core area; and (b) 50% core area.

distribution of the cross talk is less important. The number of guided modes scales up with the number of fibers, and the run time scales up quadratically with the number of fibers. As long as the confinement of fibers is the goal of modeling, a smaller number of fibers and modes may be calculated for modeling depending on the illumination conditions. In the following numerical analysis we used 5 × 5 arrays to assess confinement and kept the number of included modes sufficiently large for accurate results.

C. Introducing Irregularity in the Model

Due to lower refractive index contrast between core and extramural absorber, the actual size of the absorber material cannot be measured from the SEM image and the absorber material was excluded from the model. The modes of the waveguide array were calculated at a wavelength of 612 nm. Figure 11(a) shows the transmitted beam intensity from a perfectly regular 1.5 μm pitch waveguide array with core width of 84% fiber pitch after 500 μm propagation. Red five-sided geometries represent the FB core boundaries and the background material is the same as fiber's cladding. The incident field is a Gaussian beam with beam radius of 0.5 μm and wavelength of 612 nm launched into the central fiber at [0, 0].

Transmitted beam is not confined in the launched core due to thinner cladding width at the fixed wavelength, which makes the decay of field weaker, thus increasing the cross talk between the fibers. Moreover, perfectly identical fiber cores have a relatively weak confinement due to the strong coupling between them. The effect of FB disorder was then studied to show that it

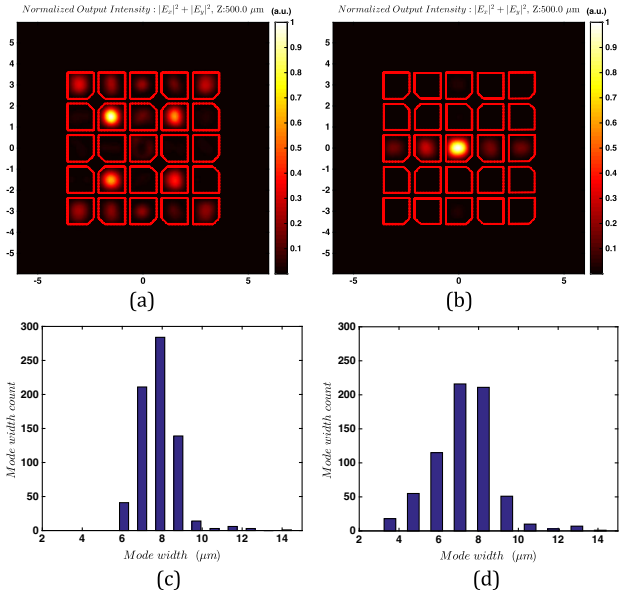

Fig. 11. Transmitted beam from (a) a regular waveguide array; and (b) irregular waveguide array with 1% variation in core width. (c) Corresponding mode count versus mode width in a regular array of fibers; and (d) irregular array of fibers.

would significantly increase the field confinement [31]. In order to accurately model imaging FBs, effects of disorder were verified numerically by introducing an irregular array of fibers. Each of the fiber core widths in the 2 × 2 fiber array [Fig. 1(d)] were reduced by 1% of the largest (original) core width in the clockwise direction starting from the upper left fiber. The rest of the fibers in the array were repeated from this disordered 2 × 2 array. Starting from the upper left fiber, the core widths are 84%, 83%, 82%, and 81% of the pitch. Figure 11(b) shows the transmitted intensity in the irregular fiber array. Because the central core width is different from its neighbors, the coupling to these fibers is also weaker, which leads to a lower cross talk.

The mode width (σ) of each guided mode is calculated for the entire modes of both regular and irregular FBs using second moment method [32]:

$$\sigma^2 = \int_{-\infty}^{+\infty} (x - x_0)^2 I(x, y)\mathrm{d}x\mathrm{d}y, \tag{6}$$

where x_0 is the center of the mode:

$$x_0 = \int_{-\infty}^{+\infty} xI(x, y)\mathrm{d}x\mathrm{d}y. \tag{7}$$

Figures 11(c) and 11(d) show the mode width count versus mode width for both the regular and irregular FBs. All of the guided modes in the regular FB have widths greater than 6 μm, while in the irregular FB the modes (33 count) have widths as low as 3.5 μm. Therefore, it is evident that introducing fabrication or engineered irregularities into FBs is crucial for proper modeling and higher confinement.

D. Modeling and Improvement of the Actual FB Cross Section

An SEM image of the 2.5 μm pitch FB cross section [Fig. 3(b)] was used to model the performance of an actual FB. Figure 12(a) shows the corresponding normalized transmitted

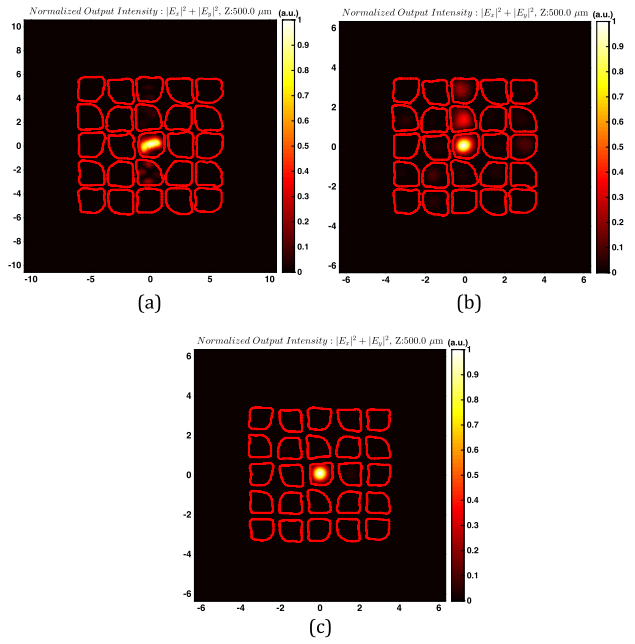

Fig. 12. Normalized transmitted intensity in (a) SEM cross section of 2.5 μm pitch FB with 70% core area; (b) same scaled cross section used for 1.5 μm pitch; and (c) numerically eroded to 50% core area with 1.5 μm pitch.

intensity. The transmitted beam is well confined within the launching core, and it is in agreement with the measurement in Fig. 5(c). The fiber irregularity associated with the FB fabrication process improves the performance of FBs in terms of cross talk. However, when the same FB structure is scaled down from 2.5 μm pitch to 1.5 μm, the irregularity is not sufficient to get the same confined optical impulse response. Instead, the modes of each fiber are more extended along the cladding, leading to a higher cross talk between fibers as seen in Fig. 12(b). One way to overcome this limitation is to increase the core–cladding refractive index contrast. However, increasing the refractive index contrast further would introduce fabrication challenges.

An alternative way to increase the FB resolution is increasing the cladding thickness so that modal field becomes weaker across the cladding, thus reducing the cross talk. In order to verify this point, the same fiber array of Fig. 12(b) was numerically eroded from 70% to 50% core area. Figure 12(c) shows

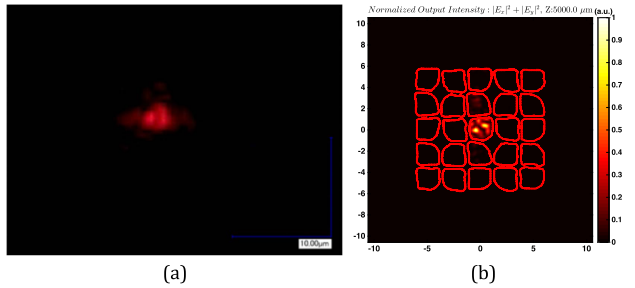

Fig. 13. Comparison of normalized intensity of (a) measured intensity; and (b) the numerical model of the 2.5 μm pitch FB for 30° angle of incidence after 5 mm propagation.

the normalized transmitted intensity of the 1.5 μm pitch FB with a 50% core area. The impulse response of the 1.5 μm pitch FB is well confined within the launch core. Therefore, a higher resolution in a FB may be achieved by increasing the cladding, at the cost of losing the light collection and increasing shift variance of the FBs. Angled illumination of the 2.5 μm pitch and 5 mm long FB with the same structure also shows high confinement as shown numerically and experimentally in Figs. 13(a) and 13(b), respectively.

5. CONCLUSION

High-resolution imaging FBs were characterized using coherent and incoherent excitations. The characterization included both measurement and numerical simulation. The measurements consisted of qualitative analysis of the image transported through different pitches of FBs, impulse response characterization of a 2.5 μm pitch FB, and finally quantitative analysis of the cross talk with incoherent collimated white light illumination.

Modal analysis was used to model the extremely deep FBs. The numerical investigation shows a relatively small number of modes, and guiding cores can be used for efficient modeling of the FBs as a guide for fabrication of high-resolution imaging FBs. As the FB pitch scales down from 2.5 to 1.0 μm, the performance of FBs gets worse at the same wavelength. This is explained by a lower confinement and larger extension of guided modes into cladding. This effect limits the resolution of the commercially available FB with NA = 1 to 2.5 μm. We proposed increasing the resolution of the FB by reducing the fill fraction of the fiber cores. Introducing disorder into the FB was shown to be crucial for improving the confinement and image resolution. One has to note that fabrication-induced disorder should be differentiated from engineered disorder. An engineered disorder may be introduced by simply choosing the initial fibers to have different core areas before the drawing process. Although the uncontrolled fabrication-induced disorder randomly varies the final shape of these fibers, the engineered disorder preserves its nature, as the core area of individual fibers remains constant. Optimization of imaging FBs using engineered and uncontrolled disorder is the topic of further investigation.

Funding. Defense Advanced Research Projects Agency (DARPA) SCENICC program (W911NF-11-C-0210).

REFERENCES

1. S.-B. Rim, P. B. Catrysse, R. Dinyari, K. Huang, and P. Peumans, "The optical advantages of curved focal plane arrays," Opt. Express **16**, 4965–4971 (2008).
2. H.-C. Jin, J. R. Abelson, M. K. Erhardt, and R. G. Nuzzo, "Soft lithographic fabrication of an image sensor array on a curved substrate," J. Vac. Sci. Technol. B **22**, 2548–2551 (2004).
3. R. Dinyari, S.-B. Rim, K. Huang, P. B. Catrysse, and P. Peumans, "Curving monolithic silicon for nonplanar focal plane array applications," Appl. Phys. Lett. **92**, 091114 (2008).
4. D. Dumas, M. Fendler, F. Berger, B. Cloix, C. Pornin, N. Baier, G. Druart, J. Primot, and E. le Coarer, "Infrared camera based on a curved retina," Opt. Lett. **37**, 653–655 (2012).
5. H. C. Ko, M. P. Stoykovich, J. Song, V. Malyarchuk, W. M. Choi, C.-J. Yu, J. B. Geddes III, J. Xiao, S. Wang, Y. Huang, and J. A. Rogers, "A hemispherical electronic eye camera based on compressible silicon optoelectronics," Nature **454**, 748–753 (2008).
6. I. Jung, G. Shin, V. Malyarchuk, J. S. Ha, and J. A. Rogers, "Paraboloid electronic eye cameras using deformable arrays of photodetectors in hexagonal mesh layouts," Appl. Phys. Lett. **96**, 021110 (2010).
7. Y. M. Song, Y. Xie, V. Malyarchuk, J. Xiao, I. Jung, K.-J. Choi, Z. Liu, H. Park, C. Lu, R.-H. Kim, R. Li, K. B. Crozier, Y. Huang, and J. A. Rogers, "Digital cameras with designs inspired by the arthropod eye," Nature **497**, 95–99 (2013).
8. T. Xie, D. Mukai, S. Guo, M. Brenner, and Z. Chen, "Fiber-optic-bundle-based optical coherence tomography," Opt. Lett. **30**, 1803–1805 (2005).
9. C. Liang, K.-B. Sung, R. R. Richards-Kortum, and M. R. Descour, "Design of a high-numerical-aperture miniature microscope objective for an endoscopic fiber confocal reflectance microscope," Appl. Opt. **41**, 4603–4610 (2002).
10. G. Oh, E. Chung, and S. H. Yun, "Optical fibers for high-resolution in vivo microendoscopic fluorescence imaging," Opt. Fiber Technol. **19**, 760–771 (2013).
11. T. S. Axelrod, N. J. Colella, and A. G. Ledebuhr, "The wide-field-of-view camera," in *Energy and Technology Review* (Lawrence Livermore National Laboratory, 1988), pp. 1–12.
12. J. Ford, I. Stamenov, S. J. Olivas, G. Schuster, N. Motamedi, I. P. Agurok, R. Stack, A. Johnson, and R. Morrison, "Fiber-coupled monocentric lens imaging," in *Imaging and Applied Optics*, OSA Technical Digest (online) (Optical Society of America, 2013), paper CW4C.2.
13. I. Stamenov, A. Arianpour, S. J. Olivas, I. P. Agurok, A. R. Johnson, R. A. Stack, R. L. Morrison, and J. E. Ford, "Panoramic monocentric imaging using fiber-coupled focal planes," Opt. Express **22**, 31708–31721 (2014).
14. A. Arianpour, N. Motamedi, I. P. Agurok, and J. E. Ford, "Enhanced signal coupling in wide-field fiber-coupled imagers," Opt. Express **23**, 5285–5299 (2015).
15. J. E. Ford, I. Stamenov, S. Karbasi, A. Arianpour, N. Motamedi, I. Agurok, R. Stack, A. Johnson, R. Morrison, J. Mott, E. Martin, C. LaReau, B. Giffel, J. Pessin, R. Tennill, and P. Onorato, "Panoramic imaging via curved fiber bundles," in *Imaging and Applied Optics*, OSA Technical Digest (online) (Optical Society of America, 2015), paper ITh1A.4.
16. S. Karbasi, A. Arianpour, N. Motamedi, W. M. Mellette, and J. E. Ford, "Quantitative analysis and temperature-induced variations of moiré pattern in fiber-coupled imaging sensors," Appl. Opt. **54**, 5444–5452 (2015).
17. K. L. Reichenbach and C. Xu, "Numerical analysis of light propagation in image fibers or coherent fiber bundles," Opt. Express **15**, 2151–2165 (2007).
18. J. H. Han and J. U. Kang, "Effect of multimodal coupling in imaging micro-endoscopic fiber bundle on optical coherence tomography," Appl. Phys. B **106**, 635–643 (2012).
19. "An Introduction to Fiber Optic Imaging," http://www.us.schott.com/lightingimaging/english/download/fo.book.pdf.
20. N. Otsu, "A threshold selection method from gray-level histograms," Automatica **11**, 23–27 (1975).
21. C. Reinsch, "Smoothing by spline functions," Numerische Mathematik **10**, 177–183 (1967).
22. S. J. Olivas, N. Nikzad, I. Stamenov, A. Arianpour, G. Schuster, N. Motamedi, W. M. Mellette, R. A. Stack, A. R. Johnson, R. Morrison, I. Agurok, and J. E. Ford, "Fiber bundle image relay for monocentric lenses," in *Computational Optical Sensing and Imaging*, OSA Technical Digest (online) (Optical Society of America, 2014), paper CTh1C.5.
23. S. J. Olivas, M. Šorel, A. Arianpour, I. Stamenov, N. Nikzad, G. M. Schuster, N. Motamedi, W. M. Mellette, R. A. Stack, A. Johnson, R. Morrison, I. P. Agurok, and J. E. Ford, "Digital image processing for wide-angle highly spatially variant imagers," Proc. SPIE **9193**, 91930B (2014).
24. S. J. Olivas, A. Arianpour, I. Stamenov, R. Morrison, R. A. Stack, A. R. Johnson, I. P. Agurok, and J. E. Ford, "Image processing for cameras with fiber bundle image relay," Appl. Opt. **54**, 1124–1137 (2015).

25. X. Chen, K. L. Reichenbach, and C. Xu, "Experimental and theoretical analysis of core-to-core coupling on fiber bundle imaging," Opt. Express **16**, 21598–21607 (2008).
26. N. Motamedi, A. Shlivinsky, J. E. Ford, and V. Lomakin, are preparing a manuscript to be called "Efficient analysis of deep high-index-contrast gratings under arbitrary illumination."
27. S.-D. Wu, T. K. Gaylord, E. N. Glytsis, and Y.-M. Wu, "Three-dimensional converging-diverging Gaussian beam diffraction by a volume grating," J. Opt. Soc. Am. A **22**, 1293–1303 (2005).
28. D. Marcuse, "Loss analysis of single-mode fiber splices," Bell Syst. Tech. J. **56**, 703–718 (1977).
29. R. van den Boomgaard and R. van Balen, "Methods for fast morphological image transforms using bitmapped binary images," CVGIP **54**, 252–258 (1992).
30. R. Adams, "Radial decomposition of disks and spheres," CVGIP **55**, 325–332 (1993).
31. S. Karbasi, K. W. Koch, and A. Mafi, "Modal perspective on the transverse Anderson localization of light in disordered optical lattices," J. Opt. Soc. Am. B **30**, 1452–1461 (2013).
32. A. E. Siegman, "How to (maybe) measure laser beam quality," in *DPSS (Diode Pumped Solid State) Lasers: Applications and Issues*, Vol. **17** of OSA Trends in Optics and Photonics (Optical Society of America, 1998), paper MQ1.